Global phenomenological optical model potential for the ^{7}Li projectile nucleus

Yongli Xu,[1,*] Yinlu Han,[2,†] Jiaqi Hu,[2] Haiying Liang,[2] Zhendong Wu,[2] Hairui Guo,[3] and Chonghai Cai[4]
[1]College of Physics and Electronic Science, Shanxi Datong University, Datong 037009, China
[2]Key Laboratory of Nuclear Data, China Institute of Atomic Energy, P.O. Box (275-41), Beijing 102413, China
[3]Institute of Applied Physics and Computational Mathematics, Beijing 100094, China
[4]Department of Physics, Nankai University, Tianjin 300071, China

(Received 29 October 2017; published 26 January 2018)

A new global phenomenological optical model potential for the ^{7}Li projectile is derived from the available experimental data of elastic-scattering angular distributions and reaction cross sections from ^{27}Al to ^{208}Pb with incident energies below 200 MeV. It is based on a smooth, unique functional form for the energy dependence of the potential depths, and physically constrained geometry parameters. The elastic-scattering angular distributions and reaction cross sections for other targets are also predicted by the obtained ^{7}Li global phenomenological optical model potential at different incident energies. These results are further compared with the corresponding experimental data. The performance shows that the ^{7}Li global phenomenological optical model potential can give a satisfactory description for ^{7}Li elastic scattering.

DOI: 10.1103/PhysRevC.97.014615

I. INTRODUCTION

The phenomenological optical model potential (OMP) successfully describing the nucleon-nucleus (NA) interaction in elastic scattering was widely used in the study of nuclear structures and nuclear astrophysics [1]. It can be obtained by assuming a form of the potential and a dependence by a number of adjustable parameters for the real and imaginary parts that vary with the projectile energy and the target mass number. In particular, the global phenomenological OMP specified for both a mass region and an energy region can reliably predict the elastic scattering observables in these regions where no measurements exist [2].

In the last few years, it has been concentrated on the study of nuclear collisions induced by stable weakly bound nuclei at energies around the Coulomb barrier [3,4]. As the weakly bound nuclei present strong cluster structures with small separation energies, the cluster structures may influence in various ways the mechanism of reactions in which they take part. Also, a large probability of breakup or transfer exists in the nuclear reactions induced by these weakly bound nuclei. Moreover, the nuclear reaction mechanisms with weakly bound stable heavy ions have been investigated and many nonconventional behaviors observed [5].

Among the reactions involving weakly bound nuclei, the lithium with its weakly bound isotopes has always interested both experimental and theoretical nuclear physicists, especially on these reactions involving the ^{7}Li incidence or emission. For example, the abundance of ^{7}Li from big bang nucleosynthesis (BBN) is one of puzzles in nuclear astrophysics [6,7]. On the other hand, the ^{7}Li nucleus exhibits an obvious cluster structure, so it can be used for probing the cluster structure of the projectile ground state [8].

With the development of the study on these reactions induced by the ^{7}Li nucleus for a range of targets, the global phenomenological OMP of ^{7}Li plays an important role to understand the complicated reaction mechanism. Recently, a large number of measurements on differential cross sections of ^{7}Li elastic scattering at different incident energies, have brought us an opportunity to investigate global OMP for it. For this purpose, we carry out systematic studies of the global OMP on ^{7}Li projectiles, which can provide information relevant to structure properties and explore the features induced by the coupled-channel effects, the breakup, and its subsequent effects of weakly bound ^{7}Li.

Up to now, the different phenomenological OMPs of ^{7}Li projectile based on the form of the Woods-Saxon potential have been given in Ref. [9], which is for individual nucleus and single incident energy. Moreover, a set of global phenomenological OMP parameters of ^{7}Li [10] has also been made for 25 sets of ^{7}Li data covering the mass range 24–208 and an energy range 28–88 MeV. However, less elastic-scattering angular distribution data and the neglected reaction cross sections in the fitting may lead to a large uncertainty of the parameters.

In this paper, a global phenomenological OMP for the ^{7}Li projectile is derived from the experimental data of the elastic-scattering angular distributions and reaction cross sections from ^{27}Al to ^{208}Pb targets with incident energies below 200 MeV. Furthermore, the elastic-scattering angular distributions and reaction cross sections are predicted for those targets outside of the mass range.

This paper is organized as follows. The basic phenomenological OMP formulas are presented and a new set of ^{7}Li global OMP parameters are given in Sec. II. The comparisons of calculated results with experimental data are shown in Sec. III. Finally, the conclusions are given in Sec. IV.

*xuyongli776@126.com
†hanyl@ciae.ac.cn

II. THE OPTICAL MODEL POTENTIAL AND PARAMETERS

A. Form of the optical model potential

The standard phenomenological OMP is defined as

$$V(r,E) = V_R(r,E) + i[W_S(r,E) + W_V(r,E)] + V_C(r), \quad (1)$$

where the first term V_R represents the real part potential, the second term W_S, and W_V are the surface and volume absorption imaginary part potential, respectively. The third term $V_C(r)$ is the Coulomb potential.

The depth of real and imaginary parts of potentials are assumed to be the Woods-Saxon type. The real part of OMP is expressed as

$$V_R(r,E) = -\frac{V_R(E)}{1+\exp[(r-R_R)/a_R]}. \quad (2)$$

The imaginary part for surface absorption of OMP is

$$W_S(r,E) = -4W_S(E)\frac{\exp[(r-R_S)/a_S]}{\{1+\exp[(r-R_S)/a_S]\}^2}. \quad (3)$$

The imaginary part for volume absorption of OMP is

$$W_V(r,E) = -\frac{W_V(E)}{1+\exp[(r-R_V)/a_V]}. \quad (4)$$

The Coulomb potential V_C is taken from the electric field of a spherical homogeneous charge density nucleus with radius R_C,

$$V_C(r) = \begin{cases} \frac{zZe^2}{2R_C}\left(3-\frac{r^2}{R_C^2}\right) & r < R_C, \\ \frac{zZe^2}{r} & r \geqslant R_C, \end{cases} \quad (5)$$

where Z and z are the charge of the target and projectile, respectively.

The potential depth is assumed to be dependent of incident energies (E in MeV),

$$V_R(E) = V_0 + V_1E + V_2E^2, \quad (6)$$

$$W_S(E) = \max\{0, W_0 + W_1E\}, \quad (7)$$

$$W_V(E) = \max\{0, U_0 + U_1E + U_2E^2\}. \quad (8)$$

The radii of these potentials are assumed to be dependent of target masses (A),

$$R_i = r_iA^{\frac{1}{3}}, \quad i = R,S,V,C, \quad (9)$$

where r_R, r_S, r_V, and r_C are the radius parameters of real part, the imaginary part of surface absorption, the imaginary part of volume absorption, as well as the Coulomb potential. The a_R, a_S, and a_V are the corresponding diffuseness width. The parameters V_0, V_1, V_2, W_0, W_1, U_0, U_1, U_2, r_R, r_S, r_V, r_C, a_R, a_S, and a_V are adjusted.

B. Parametrization of the optical model potential

The experimental data of elastic-scattering angular distributions and reaction cross sections for the ^{7}Li projectile are collected and analyzed, which include those targets for the mass 27 ⩽ A ⩽ 208 with incident energies below 200 MeV. The complete experimental databases of the elastic-scattering angular distributions and reaction cross sections for ^{7}Li is detailed in Tables I and II.

TABLE I. The $d\sigma/d\Omega$ database for ^{7}Li elastic scattering. The E_{in} is the incident energy for different targets in the laboratory system.

Target	E_{in}(MeV)	Ref.
^{27}Al	6.0,7.0,8.0,9.0,10.0,11.0,12.0,14.0,16.0,18.0	[13]
	13.0,19.0,24.0	[14]
^{28}Si	8.0,8.5,9.0,10.0,11.0,13.0,15.0,16.0	[15]
	11.5,13.0,16.0,21.0,26.0	[16]
	36.0	[17]
	177.8	[18]
^{40}Ca	34.0	[19]
	88.7	[20]
^{44}Ca	34.0	[21]
^{48}Ca	34.0	[21]
	88.7	[20]
^{46,48}Ti	17.0	[22]
^{54}Fe	36.0,42.0,48.0	[21]
^{56}Fe	34.0	[19]
^{58}Ni	14.22,16.25,18.28,19.0,20.31	[23]
	34.0	[21]
	42.0	[24]
^{60}Ni	34.0	[21]
^{62}Ni	34.0	[25]
^{65}Cu	25.0	[26]
^{64,68}Zn	34.0	[25]
^{80}Se	14.0,14.5,15.0,15.5,16.0,17.0,18.0,19.0,20.0,23.0,26.0	[5]
^{89}Y	60.0	[27]
^{90}Zr	34.0	[21]
^{116}Sn	18.0,19.0,20.0,21.0,22.0,23.0,24.0,26.0,30.0,35.0	[28]
^{120}Sn	19.5,20.5,25.0	[29]
	20.0,22.0,24.0,26.0	[30]
	28.0,30.0,44.0	[31]
^{138}Ba	21.0,22.0,23.0,24.0,28.0,30.0,32.0	[32]
	52.0	[33]
^{140}Ce	52.0	[33]
^{142}Nd	52.0	[34]
^{144}Sm	21.6,22.1,22.6,23.0,25.0,27.0,29.0,30.0,32.0,35.0,40.8	[35]
	52.0	[34]
^{208}Pb	27.0	[36]
	29.0,33.0,39.0	[37]
	42.0	[38]
	52.0	[39]

In the present work, the elastic-scattering angular distributions and reaction cross sections of ^{7}Li are fitted with the improved code APMN [11], which automatically searches global phenomenological OMP parameters on the basis of the improved fastest falling method [12] at incident energies below 300 MeV. All the potential parameter reasonable boundaries of the varied region are given by some physical limitation before the global phenomenological OMP parameters are automatically searched. The best OMP parameters are optimized with usual minimization of the χ^2, which represents the deviation of the calculated results from the experimental values. We first get the χ square for each single target and then obtain the average value of total χ square for all of the targets. The χ_i^2

TABLE II. The reaction cross section database for incident ^{7}Li.

Target	Ref.
^{27}Al	[14,50]
^{28}Si	[51–54]
$^{nat.}$Cu	[55]
^{64}Zn	[56]
^{116}Sn	[28]
^{138}Ba	[32]
^{208}Pb	[37,57]

for each target at all energy points, here i and j, respectively, indicate each target nucleus and each energy point, is defined as follows:

$$\chi^2_{i,\mathrm{el}} = \frac{1}{N_{i,\mathrm{el}}} \sum_{j=1}^{N_{i,\mathrm{el}}} \frac{1}{K_{i,j,\mathrm{el}}} \sum_{k=1}^{K_{i,j,\mathrm{el}}} \left[\frac{\sigma^{\mathrm{th}}_{i,j,\mathrm{el}}(\theta_{i,j,k}) - \sigma^{\mathrm{ex}}_{i,j,\mathrm{el}}(\theta_{i,j,k})}{\Delta\sigma^{\mathrm{ex}}_{i,j,\mathrm{el}}(\theta_{i,j,k})} \right]^2, \tag{10}$$

$$\chi^2_{i,\mathrm{re}} = \frac{1}{N_{i,\mathrm{re}}} \sum_{j=1}^{N_{i,\mathrm{re}}} \left[\frac{\sigma^{\mathrm{th}}_{i,\mathrm{re}}(j) - \sigma^{\mathrm{ex}}_{i,\mathrm{re}}(j)}{\Delta\sigma^{\mathrm{ex}}_{i,\mathrm{re}}(j)} \right]^2. \tag{11}$$

The average value of total chi square χ^2 is

$$\chi^2 = \frac{1}{N} \sum_{i=1}^{N} \frac{W_{i,\mathrm{el}}\chi^2_{i,\mathrm{el}} + W_{i,\mathrm{re}}\chi^2_{i,\mathrm{re}}}{W_{i,\mathrm{el}} + W_{i,\mathrm{re}}}, \tag{12}$$

where $N_{i,\mathrm{el}}$ and $N_{i,\mathrm{re}}$ are energy point numbers of the experimental elastic-scattering angular distributions and reaction cross sections for the ith nucleus. $K_{i,j,\mathrm{el}}$ is the angle numbers of the experimental elastic-scattering angular distributions. The superscripts th and ex represent the theoretically calculated value and the experimental value, respectively. $\sigma_{i,j,\mathrm{el}}(\theta_{i,j,k})$ and $\sigma_{i,\mathrm{re}}(j)$ are the elastic-scattering angular distributions for the kth outgoing angle and reaction cross sections, as well as $\Delta\sigma$ is the experimental error of corresponding data. $W_{i,\mathrm{el}}$ and $W_{i,\mathrm{re}}$ are the weight of the experimental elastic-scattering angular distributions and reaction cross sections for the ith nucleus. At the beginning of optimizing, the weight factors $W_{i,\mathrm{el}}$ and $W_{i,\mathrm{re}}$ both are taken as 1. N is the number of the considered nuclei.

On the basis of the elastic-scattering angular distributions in the mass range $27 \leqslant A \leqslant 208$, as well as using the improved optimization procedure, the global phenomenological OMP parameters for the ^{7}Li projectile are obtained and listed in Table III.

TABLE III. The global phenomenological OMP parameters for ^{7}Li projectile.

Parameter	Value	Unit
V_0	181.658	MeV
V_1	−0.0255	
V_2	−0.000627	
W_0	40.506	MeV
W_1	−0.125	
U_0	11.092	MeV
U_1	0.317	
U_2	−0.000223	
r_R	1.188 ($A \leqslant 100$)	fm
	1.238 ($A > 100$)	fm
r_S	1.182	fm
r_V	1.593	fm
a_R	0.852	fm
a_S	0.869	fm
a_V	0.598	fm
r_C	1.802	fm

III. CALCULATED RESULTS AND ANALYSIS

In this section, we first analyze the global OMP for the ^{7}Li projectile. Then, the elastic-scattering angular distributions and reaction cross sections are calculated using the obtained global phenomenological OMP for ^{7}Li in the target mass range $27 \leqslant A \leqslant 208$ below 200 MeV. These results are further compared with the corresponding experimental data. Finally, the elastic-scattering angular distributions and reaction cross sections are predicted for those targets outside of mass range.

The radial dependencies on the real part and imaginary part of global OMP are calculated for different targets at incident energies of 20, 100, 150, 200, 250, and 300 MeV. The results for ^{58}Ni are displayed in Fig. 1. It is found that the depth of real part potential decreases with increasing radius and incident energy. The absolute value of imaginary part firstly increases and then decreases with increasing incident radius. The contribution to imaginary part of global OMP changes from the dominant surface absorption into the volume absorption with increasing incident energy.

Another important quantity in the study of OMP is the volume integral of potential. The volume integral per nucleon of OMP is defined as

$$J_V = \frac{1}{A_p A_T} \int V_R(E,\vec{r}) d\vec{r}, \tag{13}$$

$$J_W = \frac{1}{A_p A_T} \int [W_S(E,\vec{r}) + W_V(E,\vec{r})] d\vec{r}, \tag{14}$$

where A_p and A_T are the mass numbers for projectile and target, respectively.

The ^{7}Li volume integrals per nucleon of real part and imaginary part are calculated through our global phenomenological OMP for different targets. Figure 2 shows the results for ^{58}Ni. It is observed that the volume integral per nucleon of real part J_V decreases with increasing incident energy. However, the total absorption volume integral per nucleon J_W and the volume absorption per nucleon J_{W_V} increase with increasing incident energy. The volume integral per nucleon of surface absorption J_{W_S} decreases as the projectile energy increases.

So far, a large number of the elastic-scattering angular distributions have been measured for the reactions induced by ^{7}Li. First, we calculate the elastic-scattering angular distributions using the ^{7}Li global OMP for different targets at the same incident energies. These results are further compared with the existing experiment data.

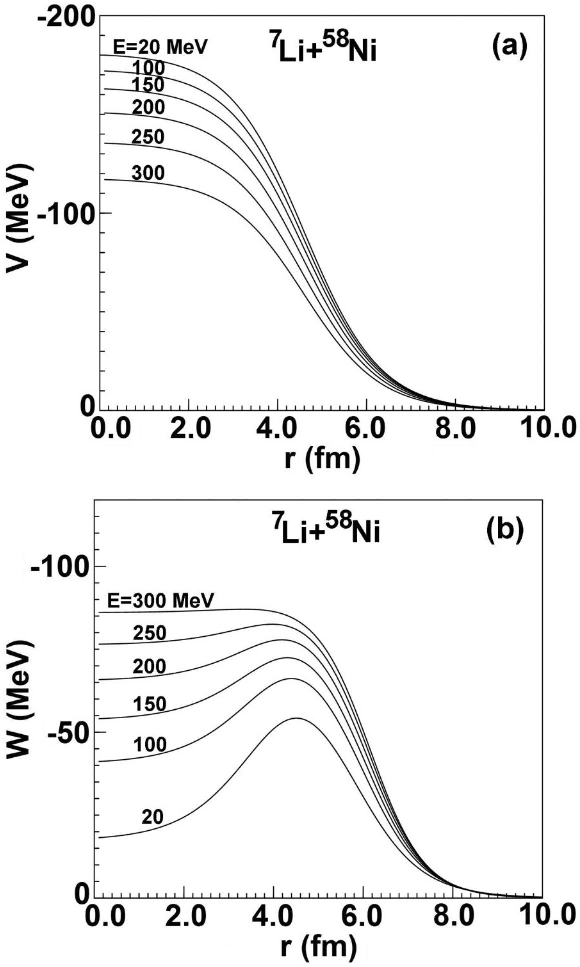

FIG. 1. The radial dependence of our global OMP at incident energies of 20, 100, 150, 200, 250, and 300 MeV for ^{58}Ni. (a) the real part; (b) the imaginary part.

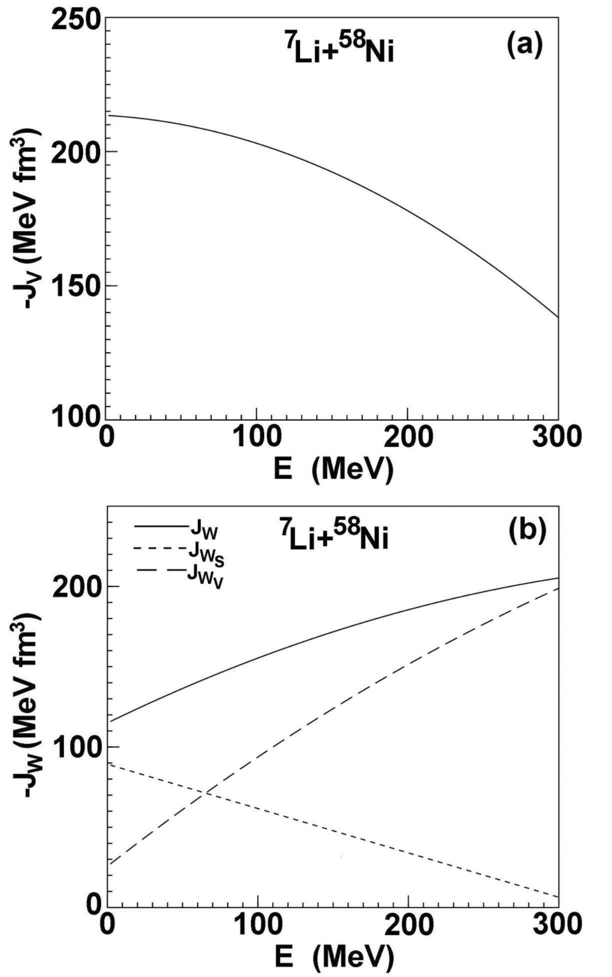

FIG. 2. Comparison between volume integrals of per nucleon for ^{58}Ni target calculated by using the ^{7}Li global OMP (solid curve) (a) the real part J_V; (b) the imaginary part J_W.

Figure 3 presents the comparisons with the experimental data in the Rutherford ratio at incident ^{7}Li energies 34.0 MeV. It is observed that this potential reproduces the elastic-scattering angular distributions data [19,21,25] well for ^{44,48}Ca, ^{56}Fe, ^{58,60,62}Ni, ^{64,68}Zn, and ^{90}Zr targets. For ^{40}Ca, there are two sets of experimental data [19,21]. The calculation is in somewhat good agreement with the experimental data from Ref. [21], and it slightly underestimates the data from Ref. [19] above 100 deg. In the same figure, the elastic-scattering angular distributions for light targets ^{11}B, ^{12,13}C, and ^{24}Mg predicted by the ^{7}Li global OMP are also presented. From the figure, one can see that the good agreements with the experimental data [40–42] are obtained except for ^{11}B and ^{12,13}C above 50 deg, where the predictions are smaller than the experimental data [40,41]. The disagreement could be from the neglect coupling effect between the elastic channel and other reaction mechanisms for these light targets. The calculations in the backward-angle area may be improved if the α cluster and sequential transfer reactions, as well as unconsidered contributions of inelastic channels were taken into account in the calculations [43,44]. Moreover, more significant influence from the nuclear structure effect may present for these light targets. This aspect needs to be investigated further.

The elastic-scattering angular distributions at incident ^{7}Li energies 52.0 MeV are calculated for ^{138}Ba, ^{140}Ce, ^{142}Nd, ^{144}Sm, and ^{208}Pb. The results are shown in Fig. 4. By comparison with the experimental data, the reasonable agreements with the data [33,34] are obtained for ^{138}Ba, ^{140}Ce, ^{142}Nd, and ^{144}Sm. The calculation slightly underestimates the data [39] for ^{208}Pb at above 60 deg. For the disagreement, it should be further verified by some new experimental data.

In addition, the elastic-scattering angular distributions at incident ^{7}Li energies 88.7 MeV are also calculated for ^{40,48}Ca. The satisfactory agreements between the calculations and experimental data [20] are presented in Fig. 5. In the figure, the elastic-scattering angular distributions for light targets ^{24,26}Mg are also predicted. One can see that the good agreements with the experimental data [20] are obtained for ^{26}Mg, while there is slight overestimation at above 40 deg for ^{24}Mg.

Then, the elastic-scattering angular distributions for the same target at different incident energies are calculated by the obtained ^{7}Li global OMP.

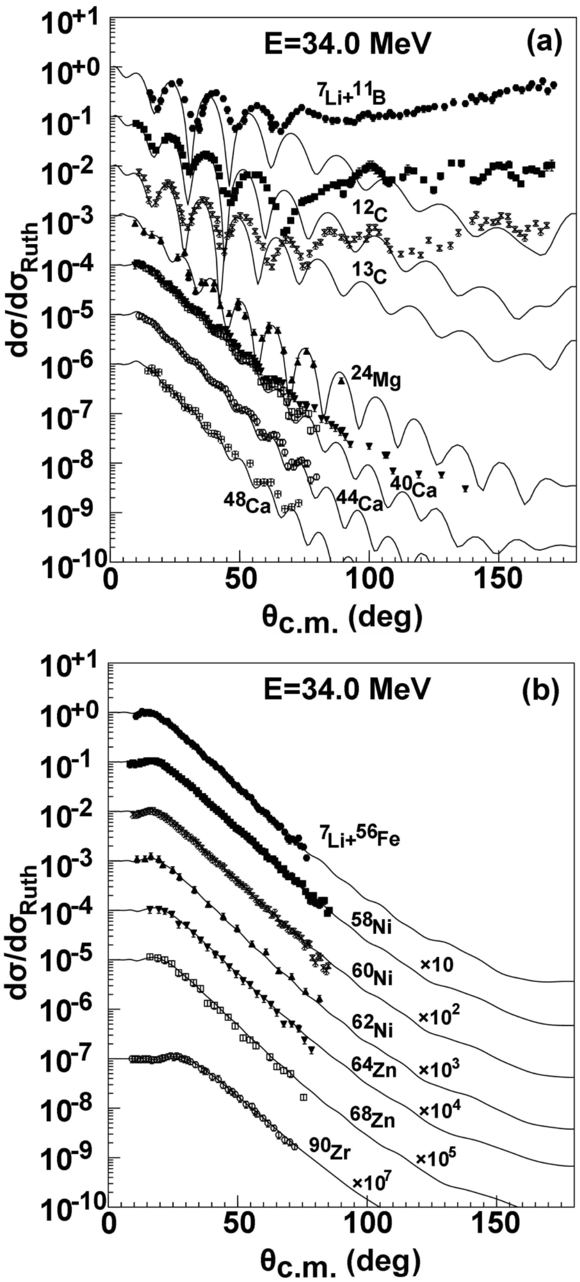

FIG. 3. Calculated elastic-scattering angular distributions in the Rutherford ratio compared with the experimental data [19,21,25,40–42] at incident ^{7}Li energies 34.0 MeV.

Figure 6 shows the comparisons with the experimental data [13,14] for ^{27}Al. The good agreements are obtained with the experimental data [14]. The calculations are also in agreement with the experimental data from Ref. [13] except for those of the incident energies 11.0 and 14.0 MeV, where there is a slight underestimation above 70 deg.

The calculations of elastic-scattering angular distributions are also compared with the experimental data [15–18] for ^{28}Si in Fig. 7. They are slightly smaller than the experimental data [15] above 100 deg, as is shown in Fig. 7(a). However, in Fig. 7(b), the good agreements with the different experimental data [16–18] are obtained below 177.8 MeV.

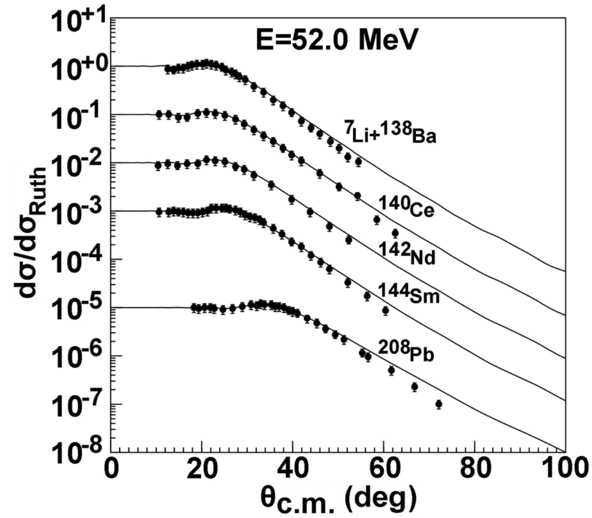

FIG. 4. Same as Fig. 3, but for 52.0 MeV [33,34,39].

In Fig. 8, the elastic-scattering angular distributions are calculated by the global ^{7}Li OMP for ^{54}Fe at incident energies 36.0, 42.0, and 48.0 MeV. The results in the Rutherford ratio are further compared with the experimental data [21]. The close agreements between them are achieved within the experimental error. Additionally, the elastic-scattering angular distributions for ^{58}Ni are also compared with the experimental data [21–24] from 14.22 to 42.0 MeV, which is shown in Fig. 9. The excellent agreement are also obtained.

In Fig. 10, the elastic-scattering angular distributions for ^{80}Se at incident energies from 14.0 to 26.0 MeV are displayed. The comparison between the calculations and the experimental data [5] reveals the reasonable agreement.

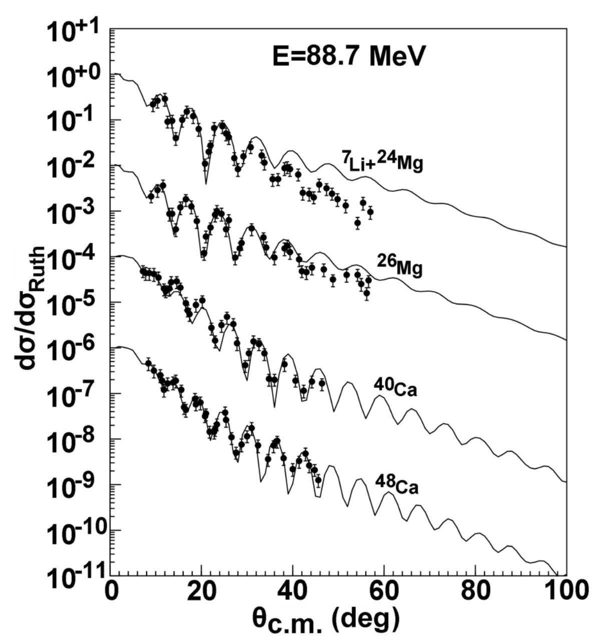

FIG. 5. Same as Fig. 3, but for 88.7 MeV [20].

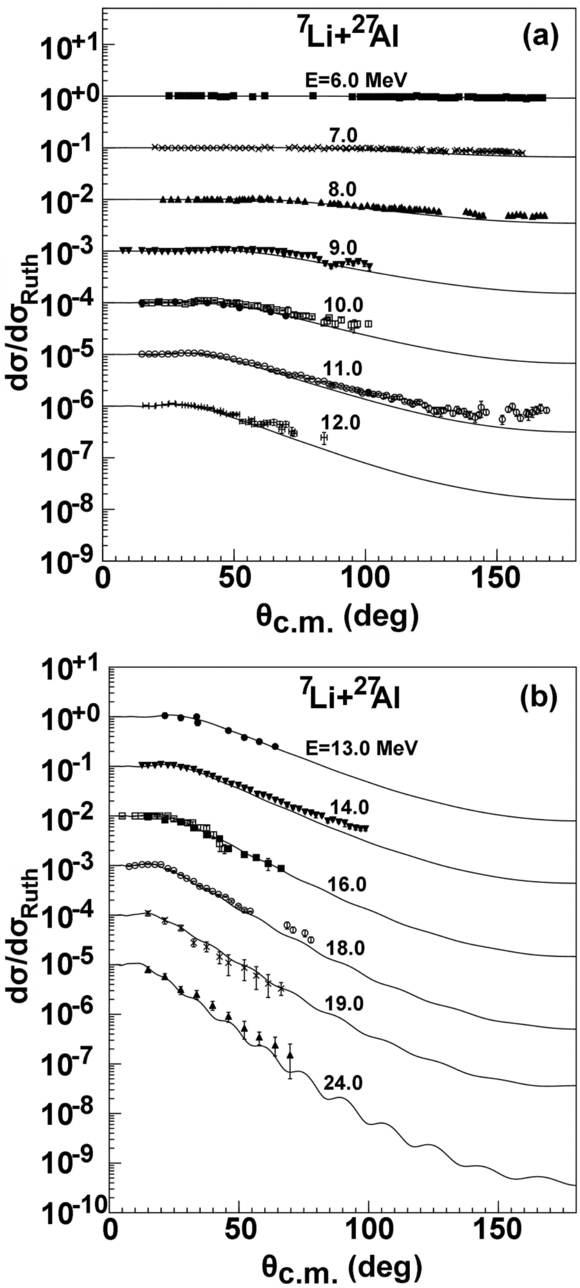

FIG. 6. Calculated elastic-scattering angular distributions in the Rutherford ratio compared with the experimental data [13,14] for ^{27}Al.

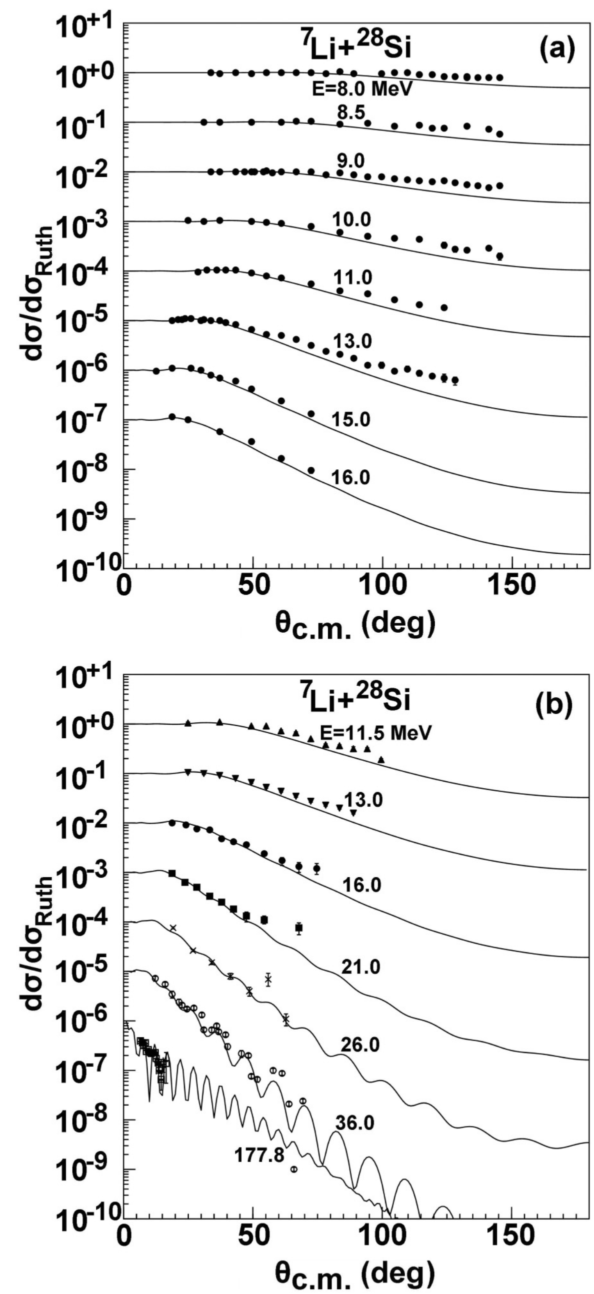

FIG. 7. Same as Fig. 6, but for ^{28}Si [15–18].

Moreover, the elastic-scattering angular distributions for some targets are measured at single incident energy. The elastic-scattering angular distributions for ^{65}Cu are calculated and compared with the corresponding experimental data [26] at incident energies 25.0 MeV, which is shown in Fig. 11. In Fig. 11, the comparisons with the experimental data [27] for ^{89}Y at incident energies 60.0 MeV are also presented. One can see that good agreements are obtained.

The elastic-scattering angular distributions for ^{116}Sn at incident energies from 18.0 to 35.0 MeV are also analyzed. The comparisons with experiment data [28] are shown in Fig. 12. It gives a slight underestimation of the experimental data [28] at incident energies from 21.0 to 26.0 MeV above 100 deg. At the other incident energies, good agreement is observed. Furthermore, we also calculate the elastic-scattering angular distributions for ^{120}Sn and compare with the latest experimental data [29–31]. However, it is clear from Fig. 12 that the calculations are in excellent agreement with the experimental data at incident energies from 19.5 to 44.0 MeV.

In Figs. 13 and 14, the elastic-scattering angular distributions for ^{138}Ba and ^{144}Sm are also obtained by the ^{7}Li global phenomenological OMP. The comparisons with experiment data [32,35] are performed for them. From these figures, one can see that this potential reproduces the elastic-scattering

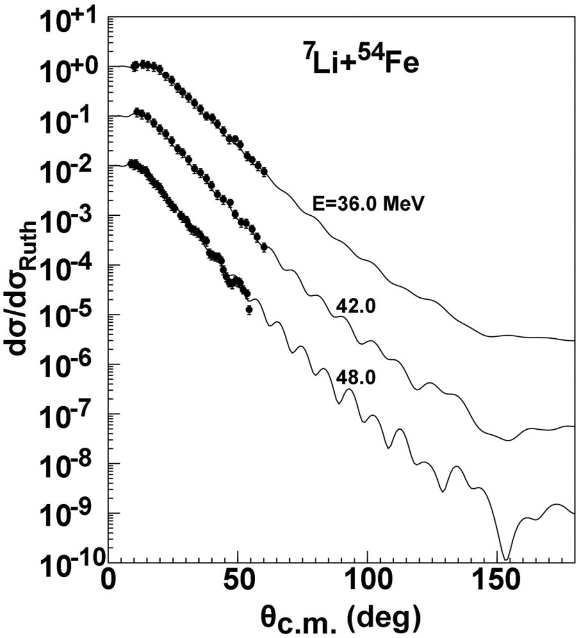

FIG. 8. Same as Fig. 6, but for ^{54}Fe [21].

angular distributions data [32] well for ^{138}Ba at incident energies from 21.0 to 32.0 MeV. The calculations are also in good agreement with the experimental data for ^{144}Sm at incident energies from 21.6 to 35.0 MeV, while the theoretical curve underestimates experimental values [35] at incident energies 40.8 MeV above 70 deg.

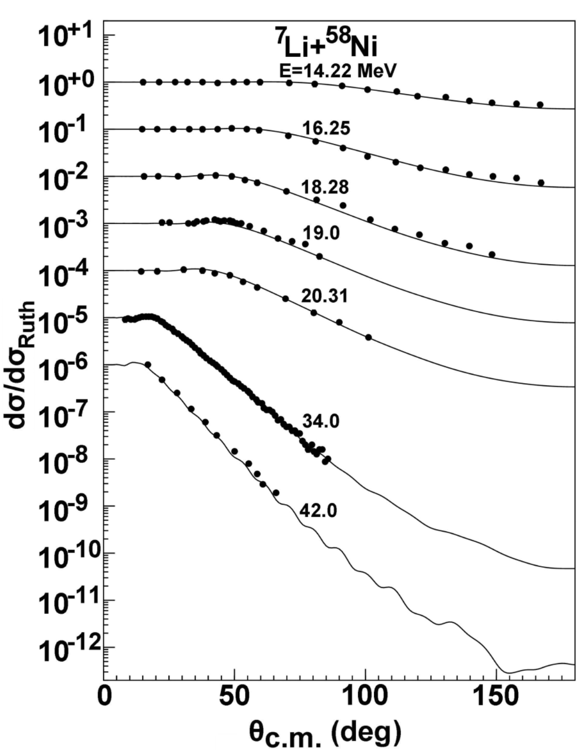

FIG. 9. Same as Fig. 6, but for ^{58}Ni [21–24].

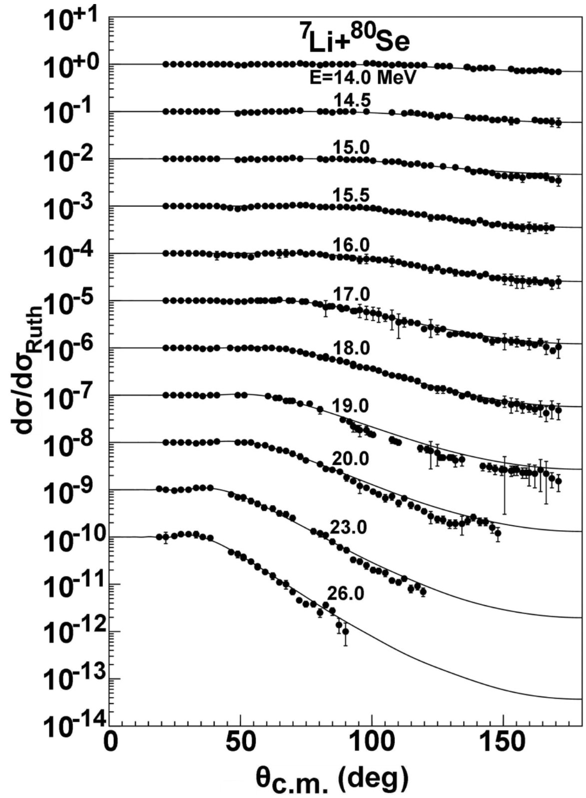

FIG. 10. Same as Fig. 6, but for ^{80}Se [5].

The calculations of elastic-scattering angular distributions for ^{208}Pb are compared with the experimental data from 27.0 to 42.0 MeV in Fig. 15. It can be observed that the calculated results well reproduce the experimental data [36,38] at incident energies 27.0 and 42.0 MeV. But the calculations underestimate the experimental data [37] at 33.0 MeV above 100 deg; unexpectedly they overestimate the data from the same experiment at 39.0 MeV.

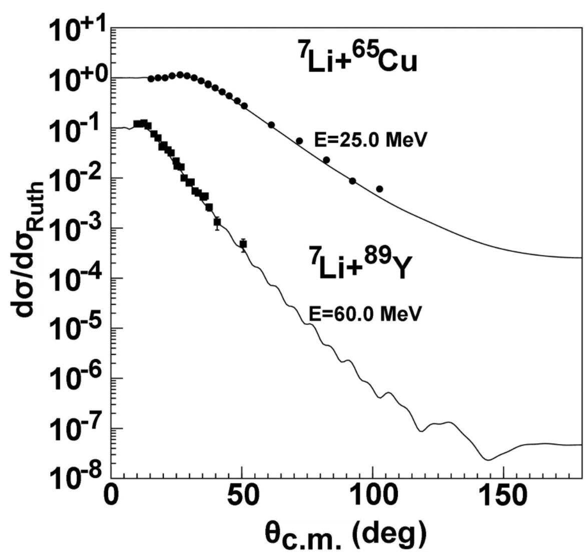

FIG. 11. Same as Fig. 6, but for ^{65}Cu and ^{89}Y [26,27].

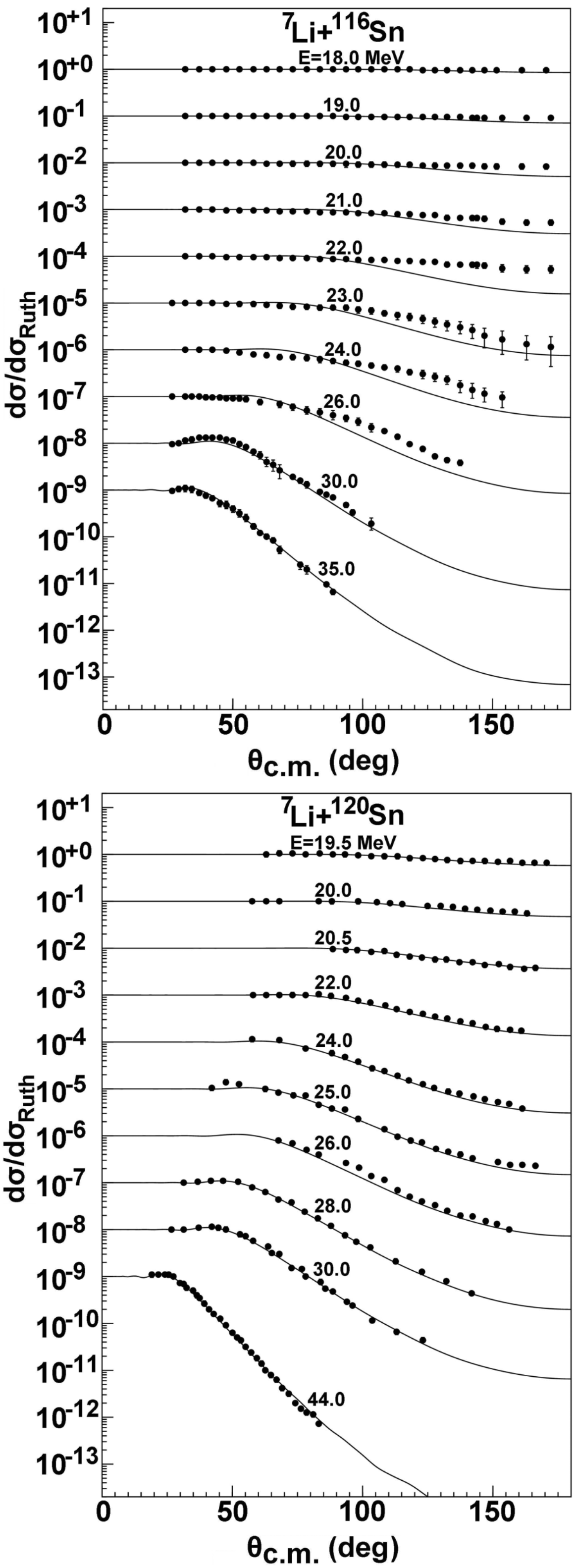

FIG. 12. Same as Fig. 6, but for ^{116}Sn and ^{120}Sn [28–31].

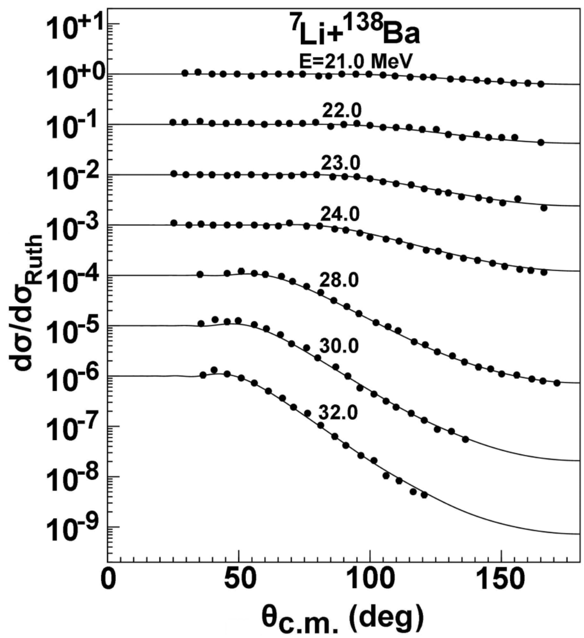

FIG. 13. Same as Fig. 6, but for ^{138}Ba [32].

Furthermore, the elastic-scattering angular distributions for some targets are measured at the same incident angle with different incident energies. The comparisons between the optical model calculations and corresponding experimental data are made for different targets.

In Fig. 16, it can be seen that the ^{7}Li OMP gives a good description of experimental data [45,46] in the error range for ^{27}Al at incident angles 140.0 and 165.0 deg. Up to now, there have been three sets of experimental data [47–49] for 170 deg. The calculated angular distributions at 170 deg are consistent with the experimental data [47,48] below about 8 MeV, while they underestimate the experimental value [49] above 8 MeV. Moreover, some experimental data at the other incident angles are given in Ref. [49] and the calculations are also compared with the corresponding data. The results are shown in Fig. 17.

The elastic-scattering angular distributions for ^{28}Si and ^{48}Ti are also compared with the experimental data [45,47,48] at 140 and 170 deg, as shown in Fig. 18. A good agreement is observed in the error range.

It is well known that the reaction cross section calculated with the optical model is important for the evaporation part of intranuclear cascade models and semiclassical pre-equilibrium models. All these nuclear models for the nonelastic channels rely on various ingredients, such as discrete level schemes, level densities, gamma-ray strength functions, fission barriers, etc. Partial wave analysis of elastic-scattering angular distributions results in sets of phase shifts that also uniquely determine the reaction cross sections. So, the reaction cross sections are also calculated by our global OMP for different targets and they are further compared with the corresponding experimental data.

In Fig. 19, the reaction cross sections for ^{27}Al and ^{28}Si calculated by the obtained ^{7}Li global OMP are presented as well as the experimental data [14,50–54]. For ^{27}Al, only the experimental data at the incident energies below 30 MeV are available and a good agreement is obtained with the calculations. For ^{28}Si, the calculations of reaction cross sections are also consistent with the experimental data below 20 MeV and

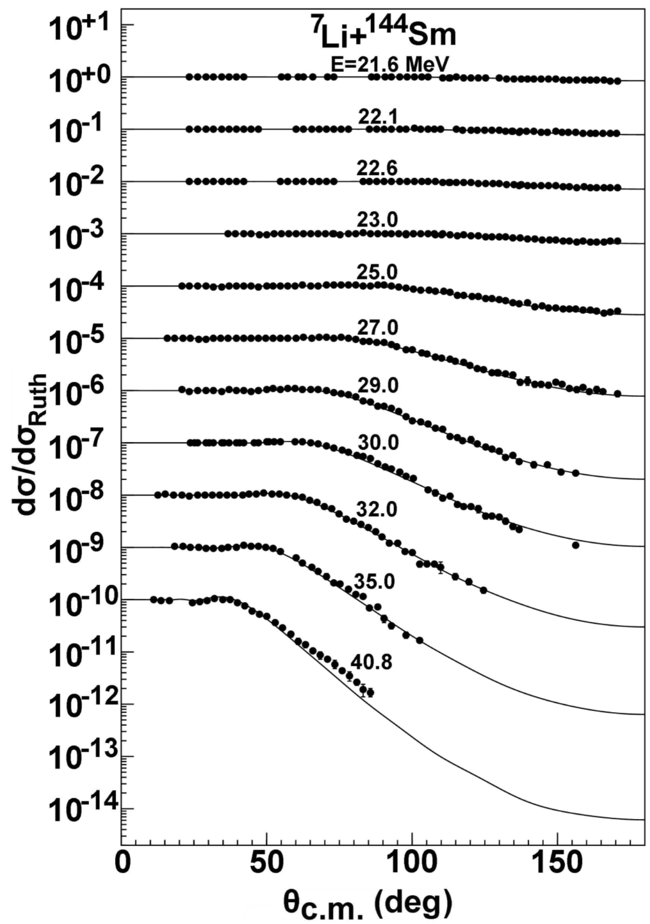

FIG. 14. Same as Fig. 6, but for ^{144}Sm [35].

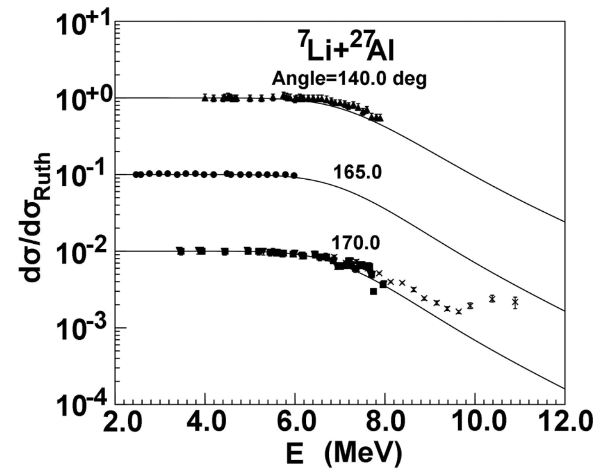

FIG. 16. Calculated elastic-scattering angular distributions in the Rutherford ratio at the same incident angle compared with the experimental data for ^{27}Al [45–49].

those of above 200 MeV are also measured. The prediction is in good agreement with the corresponding experimental data [51].

Figure 20 shows the reaction cross sections calculated by the global OMP for ^{63,65}Cu and ^{64}Zn. There are no experimental data of reaction cross sections for ^{63,65}Cu. We compare the results with the experimental data [55] of the $^{nat.}$Cu target. The reasonable agreements are achieved above 200 MeV for ^{63,65}Cu, while they are smaller than the data from the same experiment at incident energies about 160 MeV. For ^{64}Zn, it only has experimental data at incident energies 20.0 and 22.0 MeV. From the figure, it can be seen the calculations are also in excellent agreement with the experimental data [56].

The results of reaction cross sections for ^{116}Sn and ^{138}Ba are calculated by the global OMP. The comparisons with the experimental data [28] are shown in Figs. 21 and 22. One can

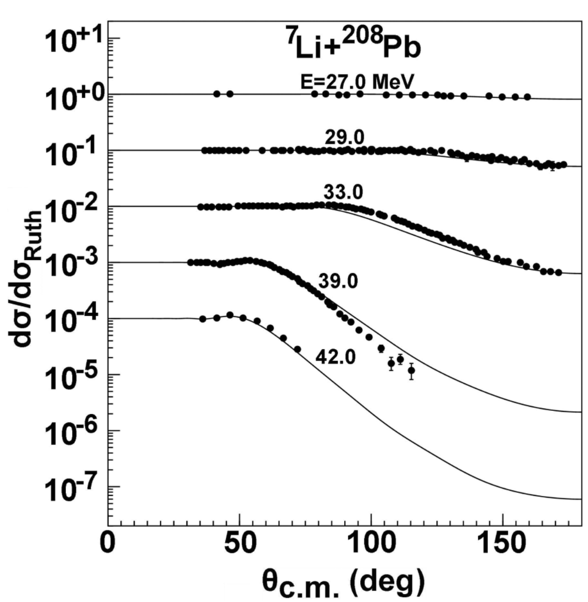

FIG. 15. Same as Fig. 6, but for ^{208}Pb [36–38].

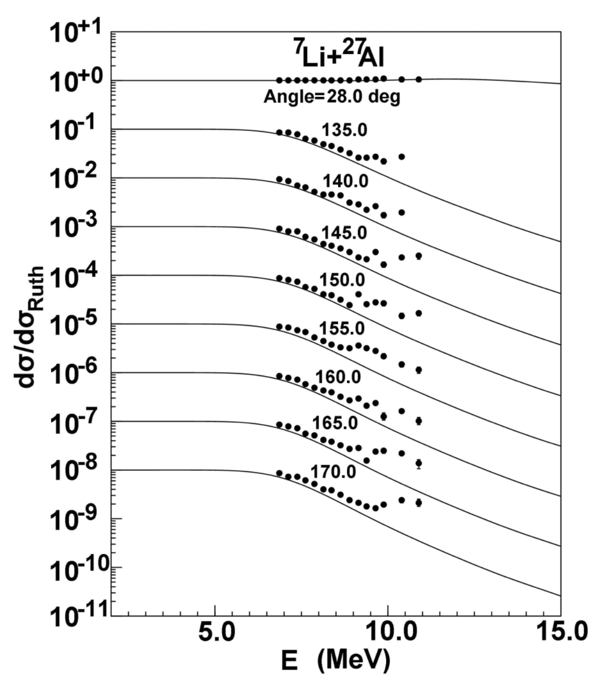

FIG. 17. Same as Fig. 16, but for other incident angles [49].

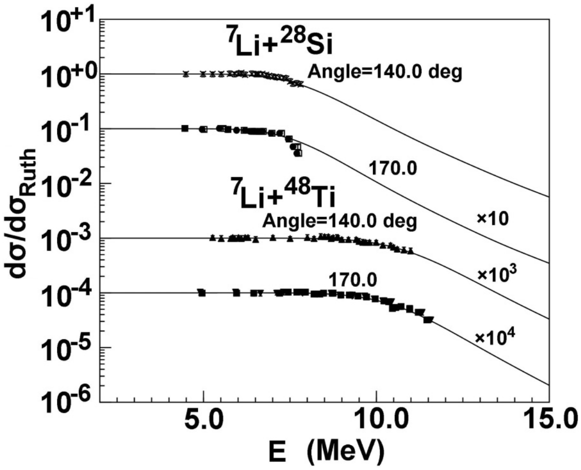

FIG. 18. Same as Fig. 16, but for ^{28}Si and ^{48}Ti [45,47,48].

see that the results are consistent with the experimental data for both targets. Furthermore, the reaction cross sections for ^{208}Pb are also compared with the corresponding experimental data [37]. The good agreements are shown in Fig. 22. Moreover, the experiment from Ref. [57] measured the reaction cross sections for $^{nat.}$Pb at incident energies 343 MeV. The comparisons between the predictions and the experimental data are performed for ^{208}Pb. The good agreement is presented in Fig. 23.

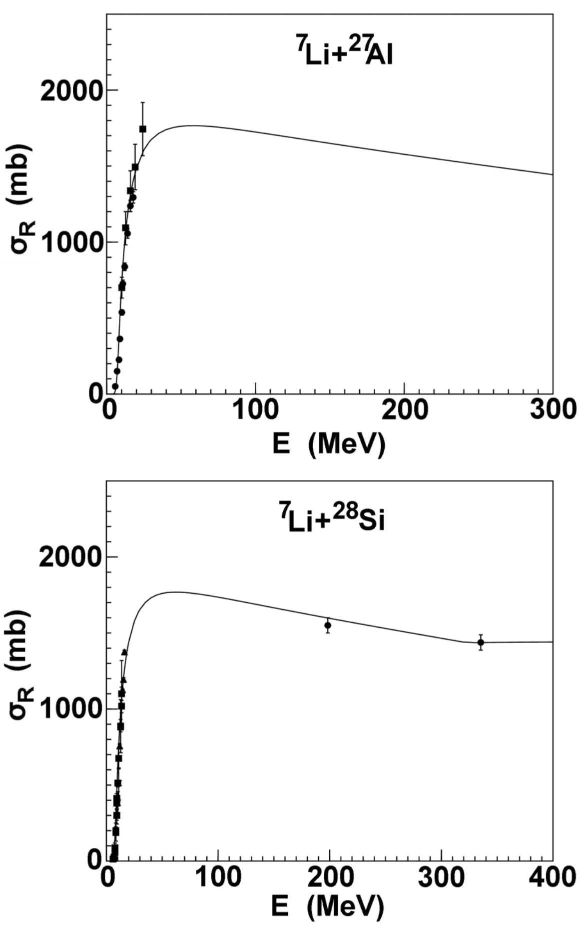

FIG. 19. Comparison between the optical model calculation and experimental data [14,50–54] of ^{7}Li reaction cross sections for ^{27}Al and ^{28}Si.

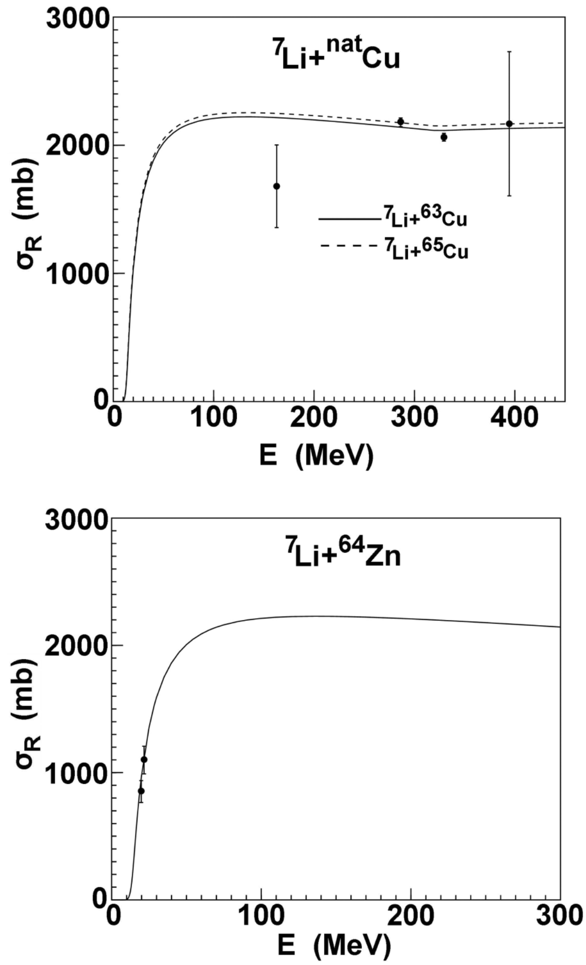

FIG. 20. Same as Fig. 19, but for $^{nat.}$Cu and ^{64}Zn [55,56].

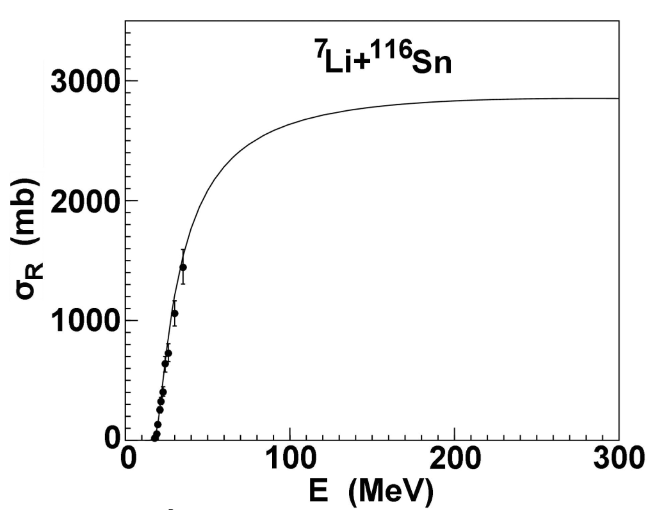

FIG. 21. Same as Fig. 19, but for ^{116}Sn [28].

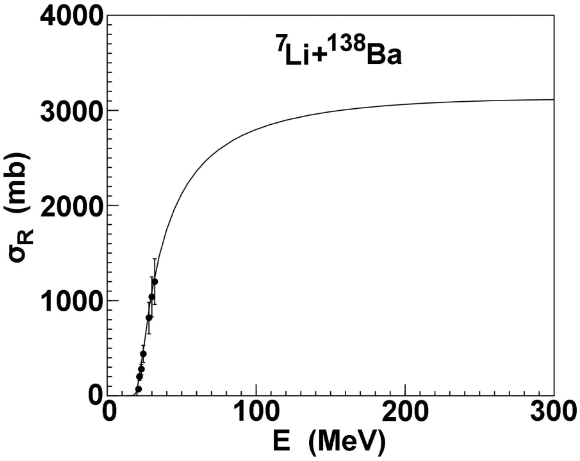

FIG. 22. Same as Fig. 19, but for ^{138}Ba [32].

From the above figures, it is revealed that there is a common tendency that the reaction cross sections for heavy nuclei increase with increasing incident energy from Coulomb barrier up to 200 MeV. However, they increase first, and then slightly decrease with increasing incident energy for light targets.

Finally, the observables in the target mass range $7 \leqslant A \leqslant 26$ are further predicted at incident energies below 200 MeV. The comparisons of elastic-scattering angular distributions for ^{9}Be, ^{12}C, and ^{16}O with the experimental data [17,41,58–67] are shown in Figs. 24 to 26. From these figures, the reasonable agreements can be found between them for ^{12}C at incident energies from 7.5 to 131.8 MeV. For ^{9}Be and ^{16}O, there are some discrepancies at some incident energies. It could be that some special reactions are not considered in the calculations for these lighter targets, such as the compound nucleus elastic scattering angular distributions, etc.

The calculations of elastic-scattering angular distributions for those targets in the mass range $209 < A \leqslant 239$, that is actinide nuclei, are also predicted by the ^{7}Li global OMP. In Fig. 27, the elastic-scattering angular distributions for ^{232}Th are compared with the experimental data [68] from 24.0 to 44.0 MeV. A good agreement is also observed between them.

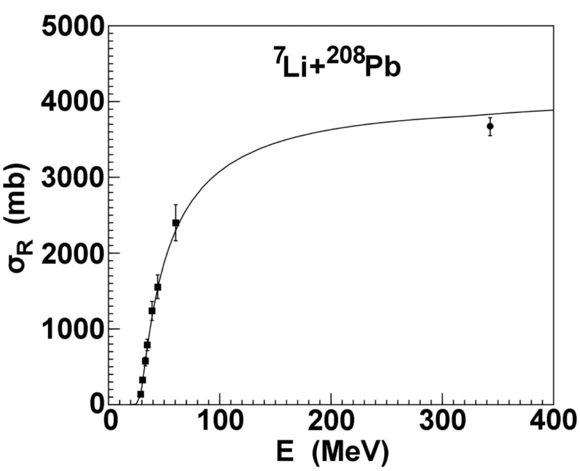

FIG. 23. Same as Fig. 19, but for ^{208}Pb [37,57].

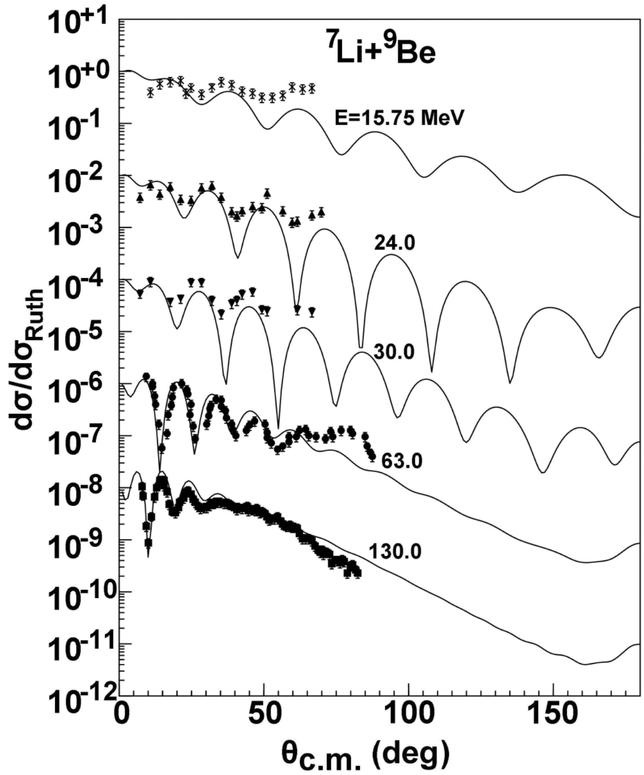

FIG. 24. Comparison between the optical model prediction and experimental data [58,59] of ^{7}Li elastic-scattering angular distributions for ^{9}Be.

Moreover, the reaction cross sections for some lighter targets are further predicted and compared with the experimental data below 200 MeV. Figure 28 gives the comparisons of

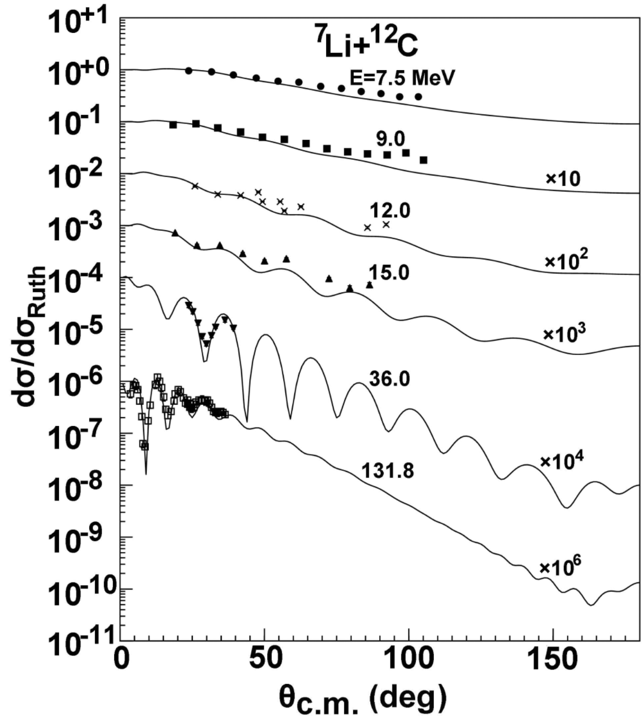

FIG. 25. Same as Fig. 24, but for ^{12}C [17,41,60–64].

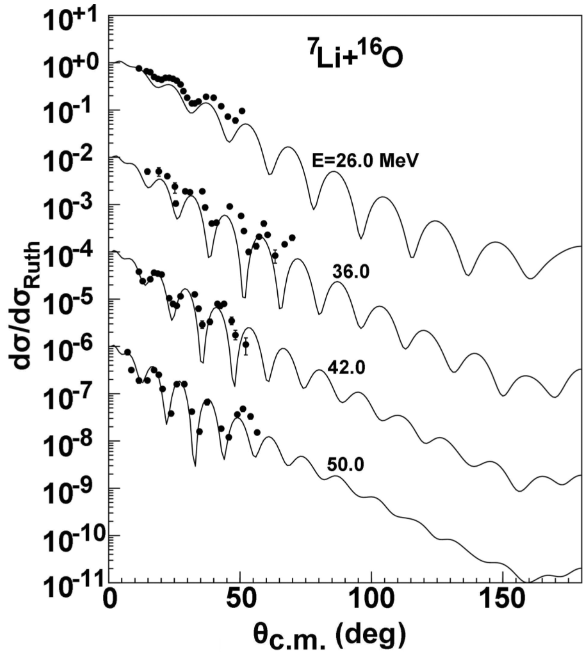

FIG. 26. Same as Fig. 24, but for ^{16}O [17,65–67].

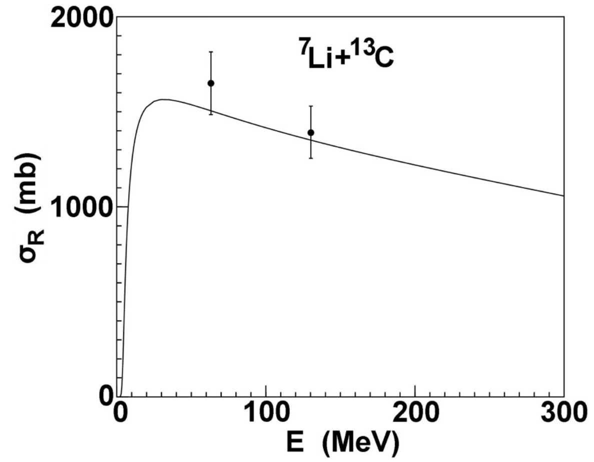

FIG. 28. Comparison between the optical model prediction and experimental data [58] of ^{7}Li reaction cross sections for ^{13}C.

reaction cross sections predicted by the obtained ^{7}Li global OMP with the corresponding experimental data [58] for ^{13}C at incident energies 63.0 and 130.0 MeV. The satisfactory agreements are shown. Similarly, the reaction cross sections for ^{9}Be also agree with the corresponding experimental data.

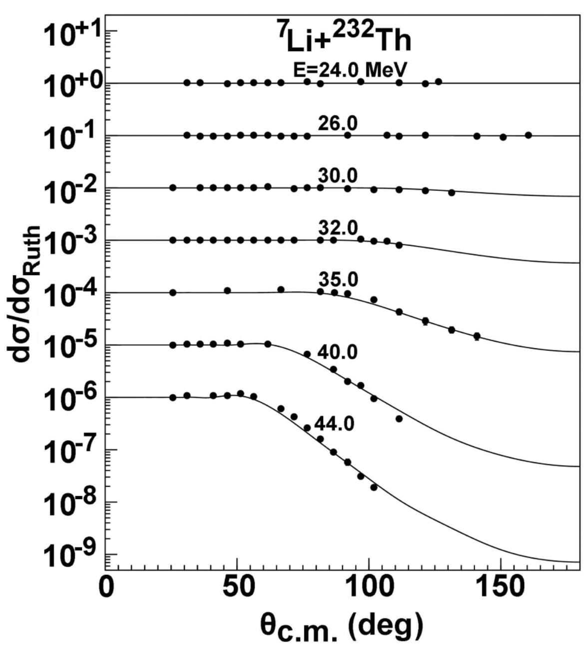

FIG. 27. Same as Fig. 24, but for ^{232}Th [68].

IV. SUMMARY AND CONCLUSIONS

We present a new set of ^{7}Li global OMP parameters for the mass range of target nuclei from 27 to 209 at incident energies below 200 MeV by simultaneously fitting the experimental data of elastic-scattering angular distributions and reaction cross sections. The comparisons and analysis are made between the calculation results and experimental data. Good agreement are obtained over the whole energy range. The predictions are also performed for the mass number of targets nuclei A < 27 and the actinide nuclei. A comparison with the experimental data shows that the predictions are also reasonable for actinide nuclei. The results of elastic-scattering angular distributions for some light targets slightly underestimate the experimental data in backward-angle area. The performed calculations reveal that the obtained ^{7}Li global OMP will be significant to investigators making systematic studies for nuclear model calculations and experimental analysis involving weakly bound nucleus ^{7}Li scattering, especially for the breakup or transfer reactions. To improve the results of the light nuclei, the best-fit OMP for them will be extracted in the next work. Moreover, the threshold anomaly at energies around the Coulomb barrier was studied for the reactions involving weakly bound projectiles in recent years. The presence of the behavior is shown that the breakup and transfer process is a very important open channel at energies around or below the Coulomb barrier. In the future work, the threshold anomaly will be discussed by the dispersion relation in detail and the other reaction mechanisms will also be further studied for the reactions involving ^{7}Li projectile.

ACKNOWLEDGMENTS

This work is supported by China National Natural Science Foundation under Grants No. 11405099 and No. 11575291. This work is also a part of IAEA Coordinated Research Projects (CRPs) on Recommended Input Parameter Library (RIPL) for Fission Cross Section Calculations under Contract No. 20464.

[1] P. E. Hodgson, *The Optical Model of Elastic Scattering* (Clarendon, Oxford, 1963).
[2] A. J. Koning and J. P. Delaroche, Nucl. Phys. A **713**, 231 (2003).
[3] P. R. S. Gomes, J. Lubian, L. F. Canto, D. R. Otomar, D. R. Mendes Junior, P. N. de Faria, R. Linares, L. Sigaud, J. Rangel, J. L. Ferreira *et al.*, Few Body Syst. **57**, 165 (2016).
[4] L. F. Canto, P. R. S. Gomes, R. Donangelo, and M. S. Hussein, Phys. Rep. **424**, 1 (2006).
[5] L. Fimiani, J. M. Figueira, G. V. Marti, J. E. Testoni, A. J. Pacheco, W. H. Z. Ca Rdenas, A. Arazi, O. A. Capurro, M. A. Cardona, P. Carnelli *et al.*, Phys. Rev. C **86**, 044607 (2012).
[6] R. Cayrel, M. Steffen, P. Bonifacio, H. Ludwig, and E. Caffau, arXiv:0810.4290v2.
[7] F. Spite and M. Spite, Astron. Astrophys. **115**, 357 (1982).
[8] A. Pakou, V. Soukeras, F. Cappuzzello, L. Acosta, C. Agodi, X. Aslanoglou, S. Calabrese, D. Carbone, M. Cavallaro, A. Foti *et al.*, Phys. Rev. C **94**, 014604 (2016).
[9] J. Cook, Atom. Data Nucl. Data Tables **26**, 19 (1981).
[10] J. Cook, Nucl. Phys. A **388**, 153 (1982).
[11] Q. B. Shen, Nucl. Sci. Eng. **141**, 78 (2002).
[12] B. Alder, S. Fernbach, and M. Rotenberg, *Methods in Computational Physics* (Academic Press, New York, 1966).
[13] J. M. Figueira, D. Abriola, J. O. Fernandez-Niello, A. Arazi, O. A. Capurro, E. De Barbara, G. V. Marti, D. Martinez-Heimann, A. J. Pacheco, J. E. Testoni *et al.*, Phys. Rev. C **73**, 054603 (2006).
[14] K. Kalita, S. Verma, R. Singh, J. J. Das, A. Jhingan, N. Madhavan, S. Nath, T. Varughese, P. Sugathan, V. V. Parkar *et al.*, Phys. Rev. C **73**, 024609 (2006).
[15] A. Pakou, N. Alamanos, G. Doukelis, A. Gillibert, G. Kalyva, M. Kokkoris, S. Kossionides, A. Lagoyannis, A. Musumarra, C. Papachristodoulou *et al.*, Phys. Rev. C **69**, 054602 (2004).
[16] M. Sinha, S. Roy, P. Basu, H. Majumdar, S. Santra, V. V. Parkar, K. S. Golda, and S. Kailas, Eur. Phys. J. C Web Conferences **17**, 03004 (2011).
[17] P. Schumacher, N. Ueta, H. H. Duhm, K.-L. Kubo, and W. J. Klages, Nucl. Phys. A **212**, 573 (1973).
[18] M. Lewitowicz, C. Borcea, F. Carstoiu, M. G. Saint-Laurent, A. Kordyasz, R. Anne, P. Roussel-Chomaz, R. Bimbot, V. Barrel, S. Dogny *et al.*, Nucl. Phys. A **562**, 301 (1993).
[19] D. P. Sanderson, S. P. Van Verst, J. Cook, K. W. Kemper, and J. S. Eck, Phys. Rev. C **32**, 887 (1985).
[20] M. F. Steeden, Jennifer Coopersmith, S. J. Cartwright, M. D. Cohler, N. M. Clarke, and R. J. Griffiths, J. Phys. G **6**, 501 (1980)
[21] C. W. Glover, R. I. Cutler, and K. W. Kemper, Nucl. Phys. A **341**, 137 (1980).
[22] T. P. Morrison, G. D. Jones, L. P. Ekstroem, F. Kearns, P. R. G. Lornie, O. M. Mustaffa, H. G. Price, D. N. Simister, P. J. Twin, and R. Wadsworth, J. Phys. G **5**, 1751 (1979).
[23] K. Zerva, A. Pakou, N. Patronis, P. Figuera, A. Musumarra, A. Di Pietro, M. Fisichella, T. Glodariu, M. La Commara, M. Lattuada *et al.*, Eur. Phys. J. A **48**, 102 (2012).
[24] D. Gupta, C. Samanta, R. Kanungo, M. K. Sharan, S. Kailas, A. Chatterjee, K. Mahata, and A. Shrivastava, Nucl. Phys. A **646**, 161 (1999).
[25] R. I. Cutler, M. J. Nadworny, and K. W. Kemper, Phys. Rev. C **15**, 1318 (1977).
[26] A. Shrivastava, A. Navin, N. Keeley, K. Mahata, K. Ramachandran, V. Nanal, V. V. Parkar, A. Chatterjee, and S. Kailas, Phys. Lett. B **633**, 463 (2006).
[27] R. Wadsworth, M. D. Cohler, M. J. Smithson, D. L. Watson, F. Jundt, L. Kraus, I. Linck, and J. C. Sens, J. Phys. G **9**, 1237 (1983).
[28] N. N. Deshmukh, S. Mukherjee, B. K. Nayak, D. C. Biswas, S. Santra, E. T. Mirgule, S. Appannababu, D. Patel, A. Saxena, R. K. Choudhury *et al.*, Eur. Phys. J. A **47**, 118 (2011).
[29] D. P. Sousa, D. Pereira, J. Lubian, L. C. Chamon, J. R. B. Oliveira, E. S. Rossi Jr., C. P. Silva, P. N. de Faria, V. Guimaraes, R. Lichtenthaler *et al.*, Nucl. Phys. A **836**, 1 (2010).
[30] V. A. B. Zagatto, J. Lubian, L. R. Gasques, M. A. G. Alvarez, L. C. Chamon, J. R. B. Oliveira, J. A. Alcantara-Nunez, N. H. Medina, V. Scarduelli, A. Freitas *et al.*, Phys. Rev. C **95**, 064614 (2017).
[31] A. Kundu, S. Santra, A. Pal, D. Chattopadhyay, R. Tripathi, B. J. Roy, T. N. Nag, B. K. Nayak, A. Saxena, and S. Kailas, Phys. Rev. C **95**, 034615 (2017).
[32] A. M. M. Maciel, P. R. S. Gomes, J. Lubian, R. M. Anjos, R. Cabezas, G. M. Santos, C. Muri, S. B. Moraes, R. Liguori Neto, N. Added *et al.*, Phys. Rev. C **59**, 2103 (1999).
[33] P. D. Clark, T. R. Ophel, J. S. Eck, A. F. Zeller, J. Nurzynski, D. C. Weisser, and D. F. Hebbard, Nucl. Phys. A **349**, 258 (1980).
[34] P. D. Clark, T. R. Ophel, J. Nurzynski, C. H. Atwood, and D. F. Hebbard, Nucl. Phys. A **352**, 267 (1981).
[35] J. M. Figueira, J. O. Fernandez Niello, A. Arazi, O. A. Capurro, P. Carnelli, L. Fimiani, G. V. Marti, D. Martinez Heimann, A. E. Negri, A. J. Pacheco *et al.*, Phys. Rev. C **81**, 024613 (2010).
[36] V. V. Parkar, V. Jha, B. J. Roy, S. Santra, K. Ramachandran, A. Shrivastava, A. Chatterjee, S. R. Jain, A. K. Jain, and S. Kailas, Phys. Rev. C **78**, 021601 (2008).
[37] N. Keeley, S. J. Bennett, N. M. Clarke, B. R. Fulton, G. Tungate, P. V. Drumm, M. A. Nagarajan, and J. S. Lilley, Nucl. Phys. A **571**, 326 (1994).
[38] D. Gupta, C. Samanta, A. Chatterjee, S. Kailas, B. J. Roy, K. Mahata, and A. Shrivastava, Nucl. Phys. A **683**, 3 (2001).
[39] A. F. Zeller, D. C. Weisser, T. R. Ophel, and D. F. Hebbard, Nucl. Phys. A **332**, 515 (1979).
[40] J. Cook, M. N. Stephens, and K. W. Kemper, Nucl. Phys. A **466**, 168 (1987).
[41] E. E. Bartosz, N. Keeley, P. D. Cathers, M. W. Cooper, K. W. Kemper, F. Marechal, and K. Rusek, Phys. Rev. C **64**, 014606 (2001).
[42] G. E. Moore, K. W. Kemper, and L. A. Charlton, Phys. Rev. C **11**, 1099 (1975).
[43] A. A. Rudchik, A. T. Rudchik, G. M. Kozeratska, O. A. Ponkratenko, E. I. Koshchy, A. Budzanowski, B. Czech, S. Kliczewski, R. Siudak, I. Skwirczynska *et al.*, Phys. Rev. C **72**, 034608 (2005).
[44] L. Yang, C. J. Lin, H. M. Jia, X. X. Xu, F. Yang, H. Q. Zhang, Z. H. Liu, P. F. Bao, and L. J. Sun, Phys. Rev. C **87**, 047601 (2013).
[45] A. Nurmela, E. Rauhala, and J. Raisanen, Nucl. Instrum. Methods B **155**, 211 (1999).
[46] M. Mayer, B. Diaz-Herrera, and M. Schneider, Nucl. Instrum. Methods B **207**, 263 (2003).
[47] J. Raisanen and E. Rauhala, Nucl. Instrum. Methods B **73**, 439 (1993).
[48] E. Rauhala and J. Raisanen, J. Appl. Phys. **75**, 642 (1994).
[49] D. Abriola, P. Carnelli, A. Arazi, J. M. Figueira, O. A. Capurro, M. A. Cardona, J. O. Fernandez Niello, D. Hojman, L. Fimiani, P. Grinberg *et al.*, Nucl. Instrum. Methods B **268**, 1793 (2010).
[50] E. A. Benjamim, A. Lepine-Szily, D. R. Mendes Jr, R. Lichtenthaler, V. Guimaraes, P. R. S. Gomes, L. C. Chamon, M. S.

Hussein, A. M. Moro, A. Arazi *et al.*, Phys. Lett. B **647**, 30 (2007).

[51] R. E. Warner, R. A. Patty, P. M. Voyles, A. Nadasen, F. D. Becchetti, J. A. Brown, H. Esbensen, A. Galonsky, J. J. Kolata, J. Kruse *et al.*, Phys. Rev. C **54**, 1700 (1996).

[52] A. Pakou, K. Rusek, N. Alamanos, X. Aslanoglou, M. Kokkoris, A. Lagoyannis, T. J. Mertzimekis, A. Musumarra, N. G. Nicolis, D. Pierroutsakou *et al.*, Eur. Phys. J. A **39**, 187 (2009).

[53] A. Pakou, K. Rusek, D. Pierroutsakou, N. Alamanos, P. A. Assimakopoulos, N. Divis, G. Doukelis, A. Gillibert, S. Harissopulos, G. Kalyva *et al.*, Phys. Rev. C **76**, 054601 (2007).

[54] A. Musumarra, P. Figuera, F. De Luca, A. Di Pietro, P. Finocchiaro, M. Fisichella, M. Lattuada, A. Pakou, M. G. Pellegriti, G. Randisi *et al.*, Nucl. Instrum. Methods A **612**, 399 (2010).

[55] M. G. Saint-Laurent, R. Anne, D. Bazin, D. Guillemaud-Mueller, U. Jahnke, Jin Gen Ming, A. C. Mueller, J. F. Bruandet, F. Glasser, S. Kox *et al.*, Z. Phys. A **332**, 457 (1989).

[56] P. R. S. Gomes, M. D. Rodriguez, G. V. Marti, I. Padron, L. C. Chamon, J. O. F. Niello, O. A. Capurro, A. J. Pacheco, J. E. Testoni, A. Arazi, M. Ramirez *et al.*, Phys. Rev. C **71**, 034608 (2005).

[57] R. E. Warner, M. H. McKinnon, N. C. Shaner, F. D. Becchetti, A. Nadasen, D. A. Roberts, J. A. Brown, A. Galonsky, J. J. Kolata, R. M. Ronningen *et al.*, Phys. Rev. C **62**, 024608 (2000).

[58] F. Carstoiu, L. Trache, R. E. Tribble, and C. A. Gagliardi, Phys. Rev. C **70**, 054610 (2004).

[59] S. Verma, J. J. Das, A. Jhingan, K. Kalita, S. Barua, K. S. Golda, N. Madhavan, P. Sugathan, S. Nath, T. Varughese *et al.*, Eur. Phys. J. A **44**, 385 (2010).

[60] M. F. Vineyard, J. Cook, K. W. Kemper, and M. N. Stephens, Phys. Rev. C **30**, 916 (1984).

[61] M. D. Cortina-Gil, P. Roussel-Chomaz, N. Alamanos, J. Barrette, W. Mittig, F. S. Dietrich, F. Auger, Y. Blumenfeld, J. M. Casandjian, M. Chartier *et al.*, Phys. Lett. B **401**, 9 (1997).

[62] V. V. Parkar, K. Mahata, S. Santra, S. Kailas, A. Shrivastava, K. Ramachandran, A. Chatterjee, V. Jha, and P. Singh, Nucl. Phys. A **792**, 187 (2007).

[63] K. Katori, T. Shimoda, T. Fukuda, S. Shimoura, A. Sakaguchi, M. Tanaka, T. Yamagata, N. Takahashi, H. Ogata, M. Kamimura, and Y. Sakuragi, Nucl. Phys. A **480**, 323 (1988).

[64] S. Jun, L. Zhi-Hong, G. Bing, B. Xi-Xiang, L. Zhi-Chang, L. Jian-Cheng, W. You-Bao, L. Gang, Z. Sheng, W. Bao-Xiang *et al.*, Chin. Phys. Lett. **27**, 052101 (2010).

[65] J. Cook, K. W. Kemper, P. V. Drumm, L. K. Fifield, M. A. C. Hotchkis, T. R. Ophel, and C. L. Woods, Phys. Rev. C **30**, 1538 (1984).

[66] A. T. Rudchik, K. W. Kemper, A. A. Rudchik, A. M. Crisp, V. D. Chesnokova, V. M. Kyryanchuk, F. Marechal, O. A. Momotyuk, O. A. Ponkratenko, B. T. Roeder *et al.*, Phys. Rev. C **75**, 024612 (2007).

[67] B. Guo, Z. H. Li, M. Lugaro, J. Buntain, D. Y. Pang, Y. J. Li, J. Su, S. Q. Yan, X. X. Bai, Y. S. Chen *et al.*, Astrophys. J. **756**, 193 (2012).

[68] Shradha Dubey, S. Mukherjee, D. C. Biswas, B. K. Nayak, D. Patel, G. K. Prajapati, Y. K. Gupta, B. N. Joshi, L. S. Danu, S. Mukhopadhyay *et al.*, Phys. Rev. C **89**, 014610 (2014).